Nanoscale

Evidence of extended cation solubility in atomic layer deposited nanocrystalline BaTiO3 thin films and its strong impact on the electrical properties

Journal:	*Nanoscale*
Manuscript ID	NR-ART-02-2018-001176.R1
Article Type:	Paper
Date Submitted by the Author:	03-May-2018
Complete List of Authors:	Falmbigl, Matthias; Institute of Physical Chemistry, University of Vienna Karateev, Igor; Kurchatov Institute Golovina, Iryna; Drexel University, Materials Science + Engineering Plokhikh, Aleksandr; Drexel University, Materials Science + Engineering Parker, Thomas; US Army Research Laboratory Vasiliev, Alexander; Russian Research Centre "Kurchatov Institute", NBIC Spanier, Jonathan; Drexel University, Materials Science + Engineering

Evidence of extended cation solubility in atomic layer deposited nanocrystalline $BaTiO_3$ thin films and its strong impact on the electrical properties

Matthias Falmbigl[1], Igor A. Karateev[2], Iryna S. Golovina[1], Aleksandr V. Plokhikh[1], Thomas C. Parker[3], Alexandre L. Vasiliev[2], and Jonathan E. Spanier[1,4,5]

[1]*Department of Materials Science & Engineering, Drexel University, Philadelphia, Pennsylvania 19104, USA*

[2]*National Research Center "Kurchatov Institute", Kurchatov Square 1, Moscow 123182, Russia*

[3]*US Army Research Laboratory, Aberdeen Proving Ground, Maryland 21005, USA*

[4]*Department of Electrical & Computer Engineering, Drexel University, Philadelphia, Pennsylvania 19104, USA*

[5]*Department of Physics, Drexel University, Philadelphia, Pennsylvania 19104, USA*

ABSTRACT

Thin films of ≈50 nm thickness with Ba/Ti-ratios ranging from 0.8 to 1.06 were prepared by depositing alternating layers of $Ba(OH)_2$ and TiO_2. Annealing at 750 °C promoted the solid-solid transformation into polycrystalline $BaTiO_3$ films containing a mixture of the perovskite and the hexagonal polymorphs with average crystallite sizes smaller than 14 nm and without impurity phases. This, together with an increase of the cubic lattice parameters for Ba-rich films suggests an extended metastable solubility range for the perovskite-phase in these nanocrystalline thin films on both sides of the stoichiometric composition. Mapping of the cation distribution utilizing energy-filtered transmission electron microscopy corroborates defect accommodation within the $BaTiO_3$ grains. While the cation off-stoichiometry in thermodynamic equilibrium is negligible for $BaTiO_3$, the metastable extended solubility range in the thin films can be directly correlated to the low annealing temperature and nanocrystalline nature. The leakage current behavior can be explained by the formation of Schottky defects for nonstoichiometric films, and the cation ratio has a distinct impact on the dielectric properties: while excess-BaO has a marginal detrimental effect on the permittivity, the dielectric constant declines rapidly by more than 50% towards the Ti-rich side. The present findings highlight the importance of compositional control for the synthesis of nanocrystalline $BaTiO_3$ thin films, in particular for low annealing and/or deposition temperatures. Our synthesis approach using alternating layers of $Ba(OH)_2$ and TiO_2 provides a route to precisely control the cation stoichiometry.

Introduction

The ever-growing demands for complex oxide thin films with enhanced dielectric constant and tunability, improved loss and leakage current, and their implementation into industrial fabrication are the driving forces behind recent developments to utilize scalable deposition methods for the synthesis of multinary oxide thin films. One of the most appealing techniques to meet these challenges is atomic layer deposition (ALD) due to an unparalleled combination of arbitrary scalability, conformal coating, and low deposition temperatures. As researchers stride towards the growth of complex, functional oxides by ALD,[1–3] one of the most pressing challenges is the precise control of the cation stoichiometry in multinary systems. As ALD utilizes low growth and processing temperatures, it can promote the formation of metastable, nanocrystalline phases, which can exhibit substantially larger solubility ranges compared to the thermodynamic equilibrium.[4] Additionally, in contrast to thin film growth techniques such as chemical solution deposition (CSD) and pulsed laser deposition (PLD), where the composition is macroscopically controlled with high precision in the precursor solution or ceramic target prior to the film growth, in ALD a rigorous calibration and control of the deposition parameters is mandatory to achieve the desired composition and functionality without detrimental influences from impurity phases.[5]

$BaTiO_3$ (BTO), which is of wide interest due to its high dielectric constant and ferroelectric nature, is prone to influences of non-stoichiometry on the resulting physical properties due to the complex phase relations in the BaO-TiO_2 system, although the solubility regime at temperatures between 1200 and 1400 °C remain within a Ba/Ti-ratio of 0.97-1.01.[6] For ceramics it was demonstrated that the dielectric constant strongly correlates with the Ba/Ti ratio due to the influence of impurity phases in both, the Ba- and Ti-rich region.[7] However, the influences on the ferroelectric phase transition are not only sensitive to the composition, but also to the sample preparation, as evident from inconsistent results observed in different studies.[7–9] These findings already point toward the existence of extended metastable solubility even in ceramics. The situation for polycrystalline thin films is even more ambiguous as only a few studies focusing on the effects of the cation ratio have been conducted: for chemical solution deposited thin films an increase of the dielectric constant at room temperature by more than a factor of 2 was observed for a sample with a Ba/Ti-ratio of 1.03 due to enhanced grain growth in comparison with the stoichiometric composition, and the Ba-rich impurity phase Ba_2TiO_4 was detected for a sample with a Ba/Ti-ratio of 1.05.[10] For semi-amorphous BTO films grown by plasma-enhanced ALD it was found that the equivalent oxide thickness (EOT) is smallest for slightly Ti-rich films, while the current density is lowest for the film with a Ba/Ti ratio of 3.[11] These findings might be correlated to the differences in the melting point in agreement with the phase diagram leading to a larger crystalline fraction of BTO in slightly Ti-rich films (Ba/Ti-ratio: 0.6-0.7).[6,11] While the influence of nanoscale size effects on the properties of BTO ceramics and thin films are thoroughly investigated,[12–16] the influence of stoichiometry on the properties of nanocrystalline BTO thin films, in particular for annealing temperatures well below 1000 °C, where the largest

differences to bulk ceramics can be expected, remains unknown. However, the strong dependence of the dielectric constant on the Ba/Ti-ratio in ceramics[7] underscores the importance of a better understanding of the factors influencing physical properties in polycrystalline thin films on the nanoscale.

Here, we apply a superlattice approach for ALD to synthesize a series of four films with alternating stacking of TiO_2 and $Ba(OH)_2$,[17] with a Ba/Ti–ratio ranging from 0.8 to 1.06. Upon annealing at 750 °C all films form polycrystalline $BaTiO_3$ containing nanocrystallites of both BTO polymorphs, the hexagonal modification and the perovskite structure, with average sizes ranging between 10 and 14 nm. X-ray diffraction and Raman spectroscopy reveal phase-pure crystalline $BaTiO_3$ with a small increase of the lattice parameter of the perovskite phase towards the Ba-rich side. However, key parameters for applications in microelectronic devices such as leakage current, permittivity and tunability vary strongly with the cation ratio, highlighting the need for precise stoichiometry control to optimize the properties of polycrystalline $BaTiO_3$ thin films.

Experimental Section

Atomic layer depositions of semi-amorphous $Ba(OH)_2$-TiO_2 laminates of ~50 nm thickness on (100) oriented silicon substrates and Pt(111)/Ti/SiO_2/Si(100) substrates (Gmek Inc.) were conducted utilizing a Picosun R200 Advanced Reactor. The cation-precursors were Absolut Ba (Air Liquide, $Ba(^iPr_3Cp)_2$), kept at 200 °C, and titanium-isopropoxide, kept at 115 °C, (Alfa Aesar, $Ti(^iOPr)_4$) during the deposition. For both of them H_2O, kept at room temperature, served as reactant. High purity N_2 gas (99.9999 %) was used as carrier gas and the growth temperature was 290 °C. The pulse and purge times were 1.6/6 s for $Ba(^iPr_3Cp)_2$ and 0.1/10 s for H_2O for the Ba-O subcycle, and 0.3/1 s for $Ti(^iOPr)_4$ and 1/3 s for H_2O for the Ti-O subcycle. An initial 12 Å thick layer of TiO_2 was deposited on all substrates to improve uniformity. While these parameters result in saturated growth for the Ti-O subcycle, the conditions for the Ba-O subcycle were found to be the best compromise between truly saturated growth conditions and the highest uniformity of the resulting thin films.[17]

Metal-insulator-metal (MIM) capacitors were produced by depositing ≈80 nm thick 90 x 90 μm^2 squares of Pt before annealing, utilizing photolithography and sputtering at room temperature for the films grown on Pt(111)/Ti/SiO_2/Si(100) substrates. *Ex-situ* annealing under an over-pressure of 5 psi O_2 was conducted using the following annealing sequence: the samples were heated to 750 °C with a rate of 4 °C/min, kept at 750 °C for 12 hours, cooled to 80 °C at a rate of 1 °C/min. A subsequent step with heating to 160 °C (3 °C/min) followed by cooling to 100 °C at a slow rate of 0.5 °C/min was applied to ensure a slow cooling through the Curie temperature of bulk $BaTiO_3$ (T_C = 123 °C).[18]

X-ray reflectivity (XRR) and grazing incidence X-ray diffraction (GI-XRD) were performed on a Rigaku Smartlab using Cu-K_α radiation. Least squares fits to the modified Bragg

equation and XRR-data fitting using the Motofit package were employed to extract film thicknesses.[19] The lattice parameters were extracted from least squares fits utilizing the WinCSD program package.[20] Surface morphologies of the films were investigated using a Zeiss Supra 50VP scanning electron microscope (SEM). Raman spectra were collected in backscattering configuration using a single monochromator (XploRA, Horiba Jobin-Yvon, Edison, NJ) and a laser (4 mW, λ = 532 nm) focused to a spot diameter of ≈10 μm at an intensity of 1.6×10^3 W/cm^2. Light was dispersed using a 2400 gr/mm grating and collected using a Peltier-cooled array detector.

Cross-sections of the MIM-capacitors for scanning transmission electron microscopy and high resolution transmission electron microscopy (STEM/HR-TEM) were prepared in a Helios (FEI, USA) Scanning Electron Microscope (SEM)/Focused Ion Beam (FIB) dual beam system equipped with gas injectors for W and Pt deposition and an Omniprobe micromanipulator (Omniprobe, USA). After depositing a 2 μm thick protective Pt layer, milling using a 30 keV Ga^+ ion beam resulted in a cross-section area of 5 × 5 μm^2, which was subsequently polished with 5 keV and 2 keV Ga^+ ion beams, respectively. These MIM-cross sections were investigated utilizing a Titan 80–300 operated at 300 kV, which is equipped with a high-angle annular dark-field (HAADF) detector (Fischione, USA), a spherical aberration (C_s) probe corrector and a post-column Gatan image filter (GIF). Digital Micrograph (Gatan, USA) and Tecnai (FEI, USA) Imaging and Analysis software were used for the image processing.

The cation ratios for all films deposited on Si-substrates were determined from Rutherford backscattering spectrometry (RBS). The backscattered alpha particle spectrometry (BAPS) data were measured utilizing an NEC Pelletron model 5SDH-2 accelerator. All measurements were conducted using a 2 MeV He^+ beam with a beam energy spread of ±1.75 keV. The sample beam current was nominally 50 nA and the total integrated beam current for each sample was about 10 μC. The RBS chamber was operated at a base-pressure of $3x10^{-8}$ Torr. The SIMNRA software package version 6.06 was used to generate RBS simulations and the Rutherford cross sections were utilized in the simulations.

The electrical properties of MIM-capacitors were measured in a probe station (Lakeshore Cryotronics TTP4) utilizing a Keithley SCS-4200 electrometer. All measurements were conducted at room temperature in air.

Results & Discussion

In order to achieve a high control over the cation ratio for the ALD-growth of $BaTiO_3$, we applied a superlattice approach growing alternating layers of TiO_2 and $Ba(OH)_2$.[17] The exact deposition sequence was $(Ti(^iOPr)_4\text{-}H_2O) \times 40 + [(4 \times (Ba(^iPr_3Cp)_2)\text{-}H_2O) \times 25 + (Ti(^iOPr)_4\text{-}H_2O) \times z] \times 10$, with z = 42, 46, 50, and 55 for the four thin films with varying Ba/Ti-ratio from 0.8 to 1.06. The individual growth rates were established from a sequence of samples with varying numbers of the two subcycles to be 0.35(2) Å for $((Ba(^iPr_3Cp)_2)\text{-}H_2O)$ and 0.30(2) Å for

($Ti(^iOPr)_4$-H_2O), respectively.[17] The XRR-scans corresponding to the four films grown on Si(100) are displayed in Fig. 1. Fits to the XRR-data based on a model shown schematically as an inset in Fig. 1 confirm the intended stacking sequences of alternating TiO_2 and $Ba(OH)_2$ layers. From the fitting results (details are provided in table S1), a constant decrease of the TiO_2 layer thickness in the superlattice scaling with the ($Ti(^iOPr)_4$-H_2O)-pulse number, z, is confirmed.

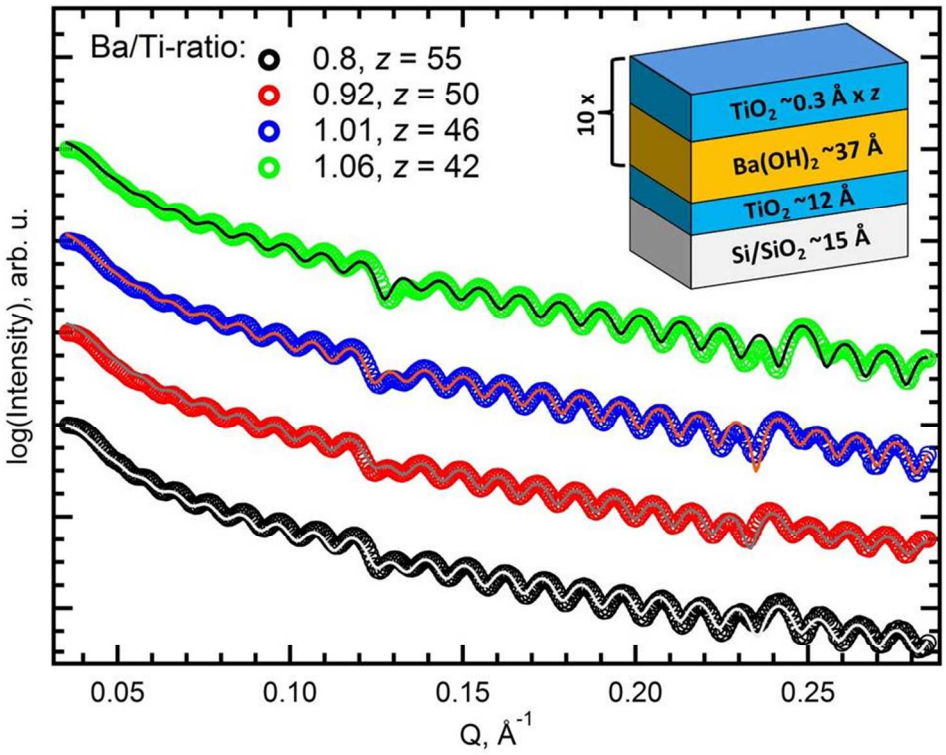

Figure 1. X-ray reflectivity data for four thin films on Si(100) with varying repeat number of ($Ti(^iOPr)_4$-H_2O), z, for the deposition sequence ($Ti(^iOPr)_4$-H_2O) × 40 + [(4 × ($Ba(^iPr_3Cp)_2$)-H_2O) × 25 + ($Ti(^iOPr)_4$-H_2O) × z] × 10. Solid lines represent fits to the depicted superlattice model.

This superlattice approach not only permits a high uniformity of ≥ 99.3 % (table 1), which was probed using 3 Si-substrate pieces distributed over a length of a 4”-wafer, but most importantly enables a fine tuning of the cation ratio. The capability to precisely adjust the cation-ratio naturally arises from the large numbers for y and z in the deposition sequence, ($Ti(^iOPr)_4$-H_2O) × 40 + [(4 × ($Ba(^iPr_3Cp)_2$)-H_2O) × 25 + ($Ti(^iOPr)_4$-H_2O) × z] × 10. Increasing or decreasing either one of these values by a small number results in a slight change in the Ba/Ti-ratio as underlined by the results presented in Fig. 2b.

Table 1. Ba/Ti-ratio (from RBS), number of Ti-O subcycles (z), film thickness, uniformity (over a length of a 4”-wafer, pseudo-cubic lattice parameter (a_{pc}), and average crystallite size extracted from HR-TEM images.

Ba/Ti-ratio	*z*, number of ($Ti(^iOPr)_4$-H_2O) repeats	film thickness, Å	uniformity, in %	average crystallite size, Å
0.80	55	517(5)	99.3	111 ± 61
0.92	50	524(5)	99.8	140 ± 58
1.01	46	493(5)	99.5	144 ± 54
1.06	42	477(5)	99.5	115 ± 46

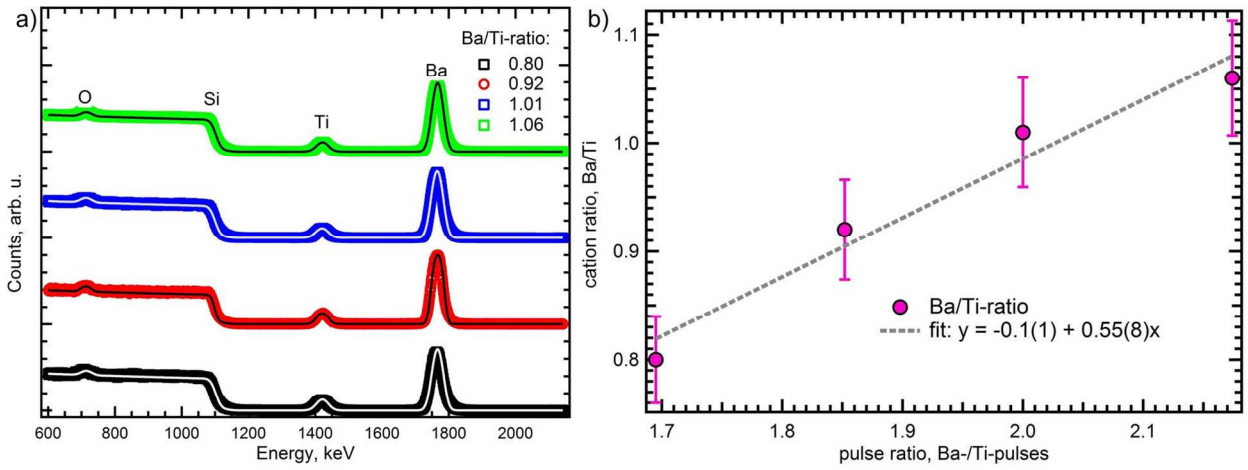

Figure. 2. a) Rutherford backscattering spectra for all four samples. b) Ba/Ti ratio determined by RBS as a function of pulse ratio of the ALD subcycles for Ba-O- and Ti-O-growth (*y*/*z*).

In the present study, we decided to vary the number of Ti-subcycles, *z*, between 42 and 55 to modify the Ba/Ti-ratio as the Ti-subcycle exhibits a smaller GPC of 0.30(2) Å and therefore permits a slightly better control over the composition. Using this approach, four samples with Ba/Ti-ratios ranging between 0.8 and 1.06 were deposited. The cation content of each sample was determined from Rutherford backscattering measurements and the corresponding spectra and models are depicted in Fig. 2a. The linear relationship between cation and pulse ratio confirms the high compositional control achieved by this superlattice approach (see Fig. 2b). The slight deviation towards a more Ti-rich composition for the sample with a Ba/Ti-ratio of 0.8 most likely arises from a slight decrease of the $Ba(^iPr_3Cp)_2$ resulting from a decreased filling level of the precursor in the source cylinder, which is corroborated by the slightly reduced GPC of 0.35 Å determined from the XRR-fits (see table S1). (This effect of a reduced but constant growth rate is specific to the setup of this ALD-system)

Gracing incidence X-ray diffraction scans, collected after annealing at 750 °C in O_2, reveal the presence of polycrystalline $BaTiO_3$ in the perovskite structure for all samples and, independent of the composition, no additional peaks are detected (Fig. 3a). The lack of impurity phases such as Ba_2TiO_4 and $Ba_{1.054}Ti_{0.946}O_{2.946}$ on the Ba-rich side, and $BaTi_2O_5$ and $Ba_6Ti_{17}O_{40}$

on the Ti-rich side in the XRD-patterns, which are typically observed in BTO ceramics and thicker films with similar deviations from stoichiometry,[6,8,10] can be attributed to the significantly lower annealing temperature of 750 °C compared to 1200 °C.[8,10] In ceramics sintered at or above 1200 °C the solubilities of BaO and TiO_2 range between Ba/Ti-ratios of 1.01 and 0.97, respectively, although the phase width varies slightly with temperature.[6,21] It is generally accepted that under oxidizing conditions Schottky disorder accounts for the change of the Ba/Ti ratio within the narrow solid solution range. The defect formation mechanism on the Ba-rich side can be described by:

(1) $$BaO \xrightarrow{BaTiO_3} Ba_{Ba}^{X} + O_O^X + V_{Ti}'''' + 2V_O^{\bullet\bullet}$$ (2.58 eV/defect)[22,23]

, and on the Ti-rich side by:

(2) $$TiO_2 \xrightarrow{BaTiO_3} Ti_{Ti}^{X} + 2O_O^X + V_{Ba}'' + V_O^{\bullet\bullet}$$ (2.90 eV/defect)[22,23]

Although only a small amount of such defects is present in thermodynamic equilibrium,[6,8] a detailed study on the grain growth of Ti-rich $BaTiO_3$ revealed that the Ba/Ti-ratio at the interfaces between grains can reach values below 0.9 implying Ti-ion segregation at the grain boundaries.[24] Furthermore, inconsistent results of the influence of non-stoichiometry on the ferroelectric phase transition in ceramics indicate the existence of metastable states of $BaTiO_3$ with enhanced solubility limits depending on the synthesis method.[7–9] For the present thin films additional factors such as the in-plane stress induced by the thermal expansion mismatch between Pt[25] and BTO[26] and a considerable contribution of grain boundaries to the total volume could promote the existence of an extended solubility range. Therefore, the segregation of excess Ba- or Ti-ions at grain boundaries as well as increased Schottky defect densities within the grains in a metastable state of BTO can be considered to account for the off-stoichiometry in the polycrystalline thin films.

The XRD diffraction patterns do not exhibit peak splitting of (*hkl*) reflections with $l \neq h,k$, which is indicative of the tetragonal ferroelectric phase (Fig. 3a). This finding is in agreement with detailed studies on fine-grained ceramics and nanoparticles, where the tetragonal lattice distortion of $BaTiO_3$ vanishes for grain sizes smaller than 100 nm.[12,14] However, the symmetry in the unit cell of BTO-nanoparticles remains tetragonal due to a small displacement of the oxygen atoms along the *c*-direction.[14] A similar scenario is expected for the nano-grained thin films, which is further corroborated by the Raman data presented below, where modes corresponding to the tetragonal phase are weaker than in bulk, but clearly present.[27]

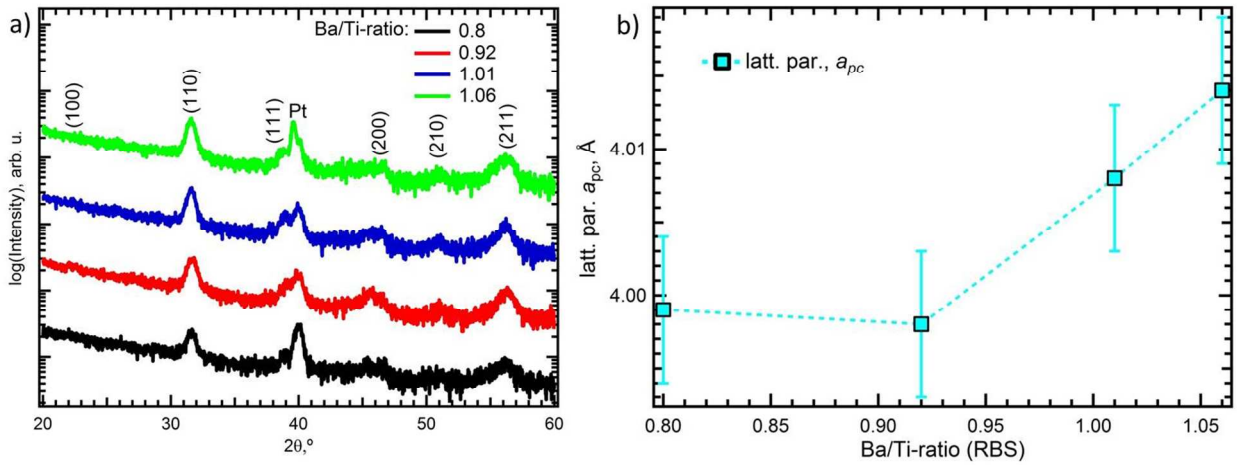

Figure. 3. a) Grazing incidence X-ray diffraction patterns of all four samples on (111)Pt/Ti/SiO_2/(100)Si substrates after annealing at 750 °C in O_2. The Bragg-indices for cubic $BaTiO_3$ (S.G.: $Pm\bar{3}m$) are provided and the (111)-peak of the Pt-substrate is marked. b) Lattice parameters (pseudo-cubic, pc) of $BaTiO_3$ as a function of Ba/Ti-ratio.

The lattice parameters extracted from least squares fits to the cubic perovskite structure (SG: $Pm\bar{3}m$) exhibit an expansion of 0.2 % with increasing Ba/Ti-ratio (table 1 and Fig. 3b). This behavior is similar to a series of Ba-rich films deposited by chemical solution deposition (CSD) on Pt-foil and annealed at 1200 °C.[10] In the latter case the cubic lattice parameters extracted from the XRD patterns reported by Ihlefeld *et. al.*[10] show an even more pronounced increase of up to 2 % with increasing Ba-content. This increase in the lattice parameter compared to the Ti-rich side could arise from the Schottky defect formation on the Ba-rich side, where in addition to each Ti-vacancy two oxygen vacancies are formed compared to only one for each Ba-vacancy on the Ti-rich side (see equations (1) and (2)). All vacancies in the perovskite lattice typically result in a local expansion due to Coulomb repulsion of the neighboring ions.[28] Therefore, the formation of three vacancies to accommodate excess BaO should result in a larger increase of the lattice parameter compared to the two vacancies introduced to the perovskite lattice on the Ti-rich side and should induce larger internal strain for the Ba-rich samples. This effect could be similar to the decrease of tetragonality found for Ba-rich ceramics.[9] Indeed, theoretical calculations on the strain produced by such defects in $SrTiO_3$ reveal that the lattice expansion towards the Ba-rich side is significant, while on the Ti-rich side depending on the nature of the defects (combined cation and oxygen vacancies or isolated vacancies) the crystal lattice either expands or contracts with a much smaller rate as a function of off-stoichiometry.[29]

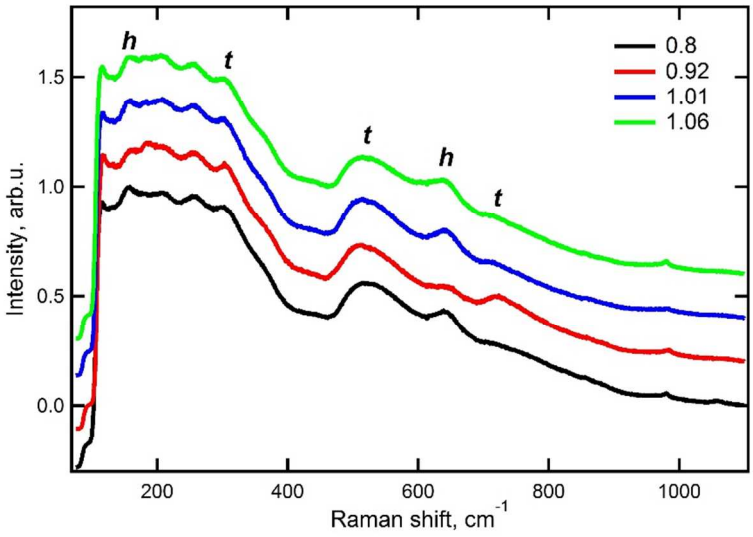

Figure. 4. Raman spectra of all samples on (111)Pt/Ti/SiO_2/(100)Si substrates after annealing at 750 °C in O_2 as a function of Ba/Ti-ratio. Characteristic modes for the tetragonal, *t*,[27] and hexagonal, *h*,[30] modification of $BaTiO_3$ are indicated.

To elucidate the presence of different $BaTiO_3$ polymorphs (hexagonal and perovskite structure) and the crystal symmetry of the $BaTiO_3$ perovskite phase, Raman spectra were collected and are displayed in Fig. 4. All samples reveal polymorphism, which is, independent of the deposition technique, frequently observed for polycrystalline $BaTiO_3$ thin films and was also reported for nanoparticles with a size of 40 nm.[14,31–33] Residual carbon contaminations could be responsible for the formation of the hexagonal phase as reported for sol-gel synthesized ultra-fine particles.[34] The observation of Raman modes at 620 cm^{-1} in BTO ceramics and thin films are also associated with enhanced pressure and strain.[35,36] The sample with a Ba/Ti-ratio of 0.92 reveals the smallest fraction of the hexagonal modification and the highest intensity of the mode at 722 cm^{-1}, which signifies the tetragonally distorted ferroelectric phase of $BaTiO_3$.[27] This mode becomes less intense in the Ba-rich films and the sample with a Ba/Ti-ratio of 0.8. The observed trend is consistent with findings for BTO ceramics, where a Ba/Ti-ratio of 0.96 results in larger tetragonal distortion compared to more Ba-rich compositions.[9] Although the lattice symmetry is cubic, the presence of the modes associated with the tetragonal phase could arise from a symmetry reduction similar to 40 nm $BaTiO_3$ particles initiated by a small displacement of the oxygen atoms.[14] The stoichiometric sample still exhibits some intensity at 722 cm^{-1}, whereas this mode vanishes for larger off-stoichiometry. Moreover, the fraction of hexagonal $BaTiO_3$ increases in a similar manner in both compositional directions compared to the sample with a Ba/Ti-ratio of 0.92. The presence of the high-temperature hexagonal phase, which is indicative of strain in the thin film samples, can be explained by co-crystallization of both polymorphs and slow kinetics of the reconstructive reaction, which is required to transform this metastable phase into the thermodynamically stable perovskite structure. This finding clearly demonstrates that for

all thin film samples a metastable state is accessed after a temperature induced solid-solid transformation from the semi-amorphous as-grown films at 750 °C.

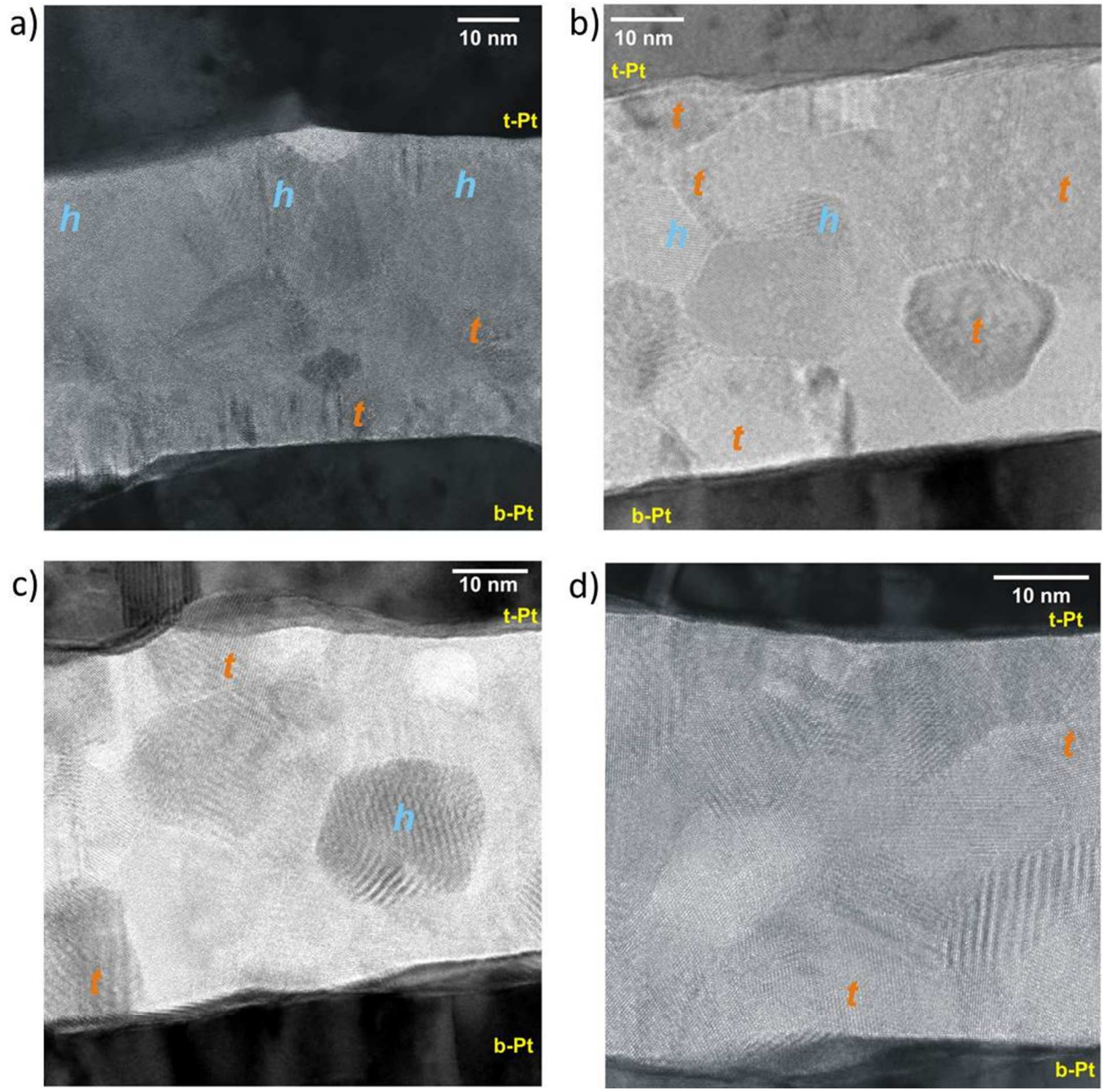

Figure. 5. BF-TEM cross sections of the MIM-structures after annealing at 750 °C for Ba/Ti-ratios of a) 0.80, b) 0.92, c) 1.01, and d) 1.06. t-Pt and b-Pt denote the top and bottom Pt-electrodes and *t* and *h* indicate crystallites of the tetragonal or hexagonal polymorph of $BaTiO_3$, respectively.

Cross sections of the MIM-capacitors for all samples were examined between the top- and bottom-electrodes to gain a better understanding of the structural and morphological influences

on the resulting physical properties. Representative BF-TEM images are depicted in Fig. 5. In all cases well-crystallized $BaTiO_3$ films with random orientation of the grains are observed between the electrodes. Crystallites of the tetragonal and hexagonal polymorphs, which were identified by fast Fourier transformation (FFT) of non-overlapping grains, are randomly distributed indicating that a co-crystallization of both phases occurs during annealing. In agreement with the GI-XRD data and Raman spectra, no impurity phases were found and no extended amorphous regions for the most Ba- or Ti-rich films were observed. The average crystallite sizes ranging between 10 and 14 nm confirming the nanocrystalline nature of these thin films were determined from HR-TEM imaging (table 1) and decrease in size with larger off-stoichiometry. The size of the BTO-grains in uncapped areas of the films estimated from the AFM-images in Fig. S1 and the SEM images in Fig. S2 exhibit a similar trend and range for all samples between 40(10) and 50(10) nm (see table S2).

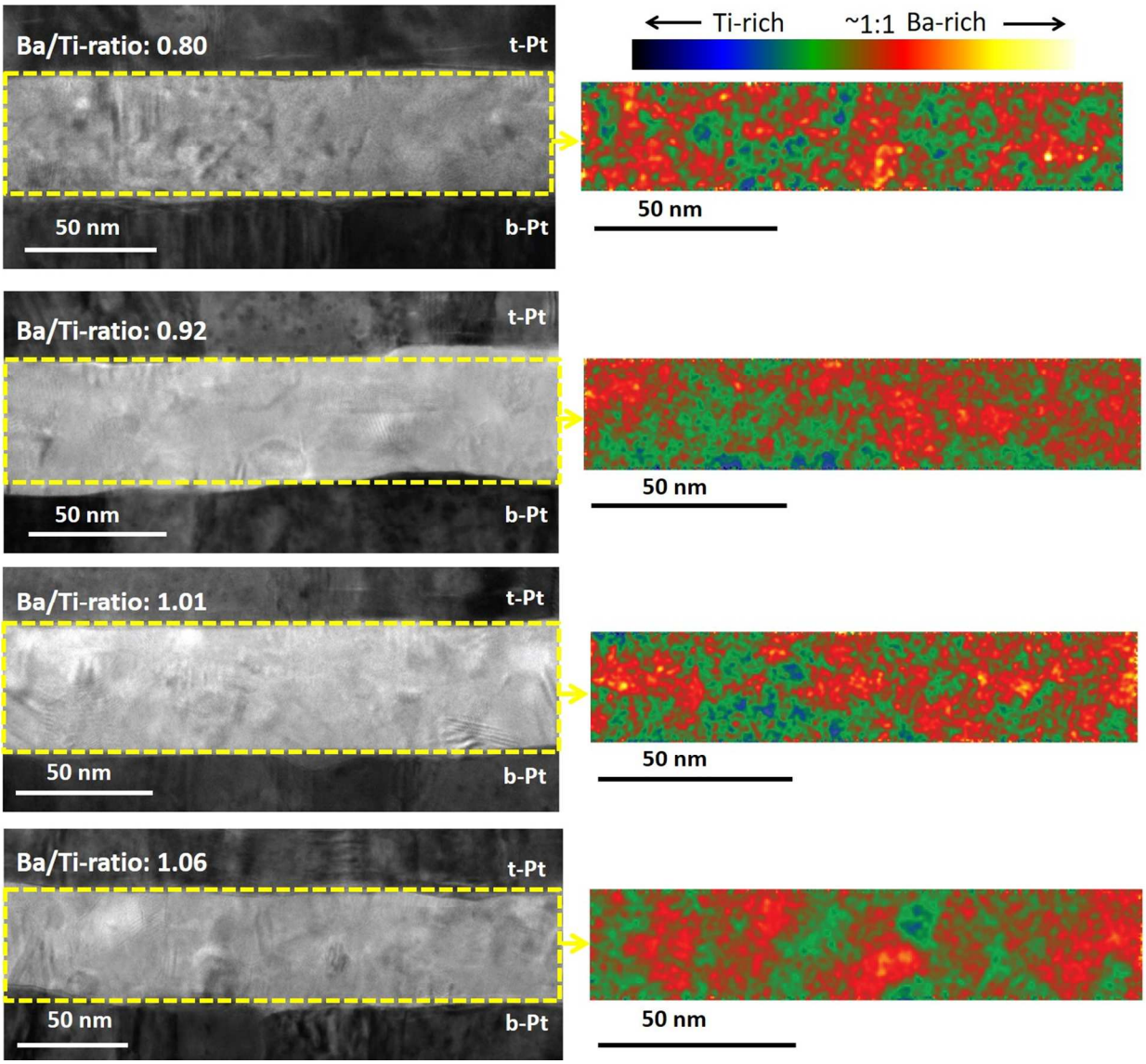

Figure. 6. EF-TEM results for cross sections of all four films collected between the Pt-electrodes. The zero-loss images are on the left side, the corresponding overlaid and color-coded concentration profiles of Ba and Ti providing qualitative information on the cation distribution are on the right side.

To examine the cation distribution within the MIM-structure, cross-sections of all four films were investigated utilizing energy-filtered TEM (EF-TEM). The results are displayed in Fig. 6. Although no quantitative information can be extracted, the images clearly show that the Ba/Ti-ratio fluctuates locally independent of the overall Ba/Ti-ratio. The presence of Ba- and Ti-enriched areas in the size of the BTO-crystallites for all compositions confirm that off-stoichiometry is not accommodated by segregation at the grain boundaries and/or by the formation of impurity phases, but by intrinsic defect formation. In general, most Ti-rich regions are located closer to the Pt-bottom electrode, while the Ba-rich areas are found predominantly towards the top of the films. As this trend applies to all films independent of the overall composition, this phenomenon could partially arise from diffusion of the Ti-adhesion layer of the substrate into the film.[37,38] In an attempt to extract information on the uniformity we fitted a Gaussian function for the Ba/Ti-ratio distribution of each sample. The full width at half maximum (FWHM) reveals a more uniform cation distribution for the most off-stoichiometric samples and the widest range for the sample with a Ba/Ti-ratios of 0.92 (see Fig. S3).

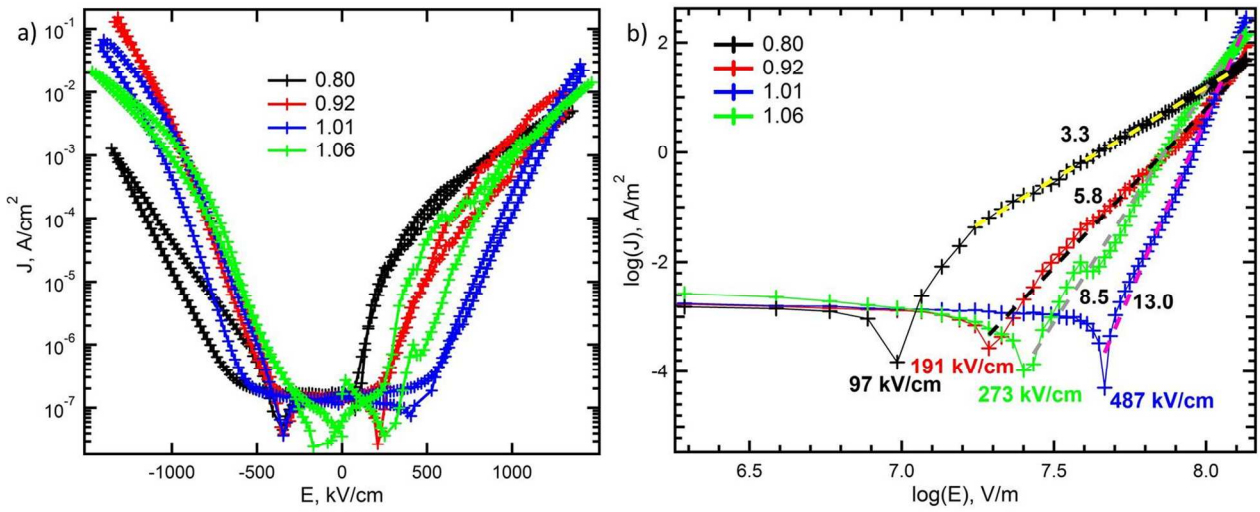

Figure. 7. a) Current density, *J*, as a function of applied electric field, *E*, for MIM-capacitors with different Ba/Ti-ratios, and b) double-log plot for the positive bias with increasing electric field. The dashed lines correspond to linear fits and the slope is provided.

The microstructural characteristics of these nanocrystalline thin films are also reflected in their leakage current behavior, which is displayed in Fig. 7a. In all cases asymmetric responses of the current density for positive and negative bias imply significant contributions from the electrode-film interfaces. Common to all films are pronounced minima prior to a steep increase

of the current density, which can be attributed to transient conductivity.[39] It is apparent that the leakage current changes systematically as a function of the composition. Therefore, an analysis of the conduction mechanisms was performed considering the interface-limited Schottky mechanism,[40] the modified Schottky mechanism proposed by Simmons,[41] which is applicable to insulators with an electronic mean-free path shorter than the film thickness and comprises contributions from bulk (mobility) as well as from the interface (free carriers), and the bulk-limited Poole-Frenkel mechanism.[42] If one of these mechanisms dominates, the slope of the corresponding linear field dependence should reflect the optical dielectric constant of ~4 for $BaTiO_3$.[43] None of the samples exhibits Poole-Frenkel dominated conduction in the positive or negative bias regime, which can be expected for thin oxide films.[44] Also the simple Schottky-mechanism was ruled out for all MIM-structures. In fact, only for the sample with a Ba/Ti-ratio of 0.8 an optical dielectric constant of 4.2 close to the expected value of 4 was found for the positive bias using the modified Schottky model (Fig. S4). This finding suggests that in very Ti-rich films a Schottky barrier is present when the electrons are injected from the bottom electrode, while in all other cases various mechanisms contribute to the conduction. However, the systematic change of the onset electric field for the steep increase in current density can be explained by the formation of Schottky-defects in off-stoichiometric samples (Fig. 7b): the sample with a Ba/Ti-ratio of 1.01 has the largest onset field, which decreases in both directions indicating that donor and acceptor states are formed in the band gap; hence lowering the energy required for electrons to access the conduction band. Accordingly, also the slope of the current density in Fig. 7b constantly decreases as the composition diverges from stoichiometry, which suggests that the scattering of electrons by these ionic impurities is enhanced. This behavior is distinctly different from semi-amorphous $BaTiO_3$ thin films grown by plasma-enhanced (PE) ALD, where the current density increases several orders of magnitude for Ti-rich films.[11]

Table 2. Ba/Ti-ratio (from RBS), dielectric constant, ε, at 0 $kVcm^{-1}$ and 100 kHz, tunability, n, at +1300 $kVcm^{-1}$ and 100 kHz, equivalent oxide thickness (EOT), and the anharmonic coefficient, α, for the field dependence of the dielectric constant after Johnson.[45]

Ba/Ti-ratio	ε	n	***EOT*, nm**	α, **cm^2kV^{-2}**
0.80	79.3	1.44	2.54	8.2×10^{-13}
0.92	109.3	1.73	1.87	6.0×10^{-13}
1.01	161.6	2.21	1.19	4.2×10^{-13}
1.06	160.8	2.18	1.16	4.0×10^{-13}

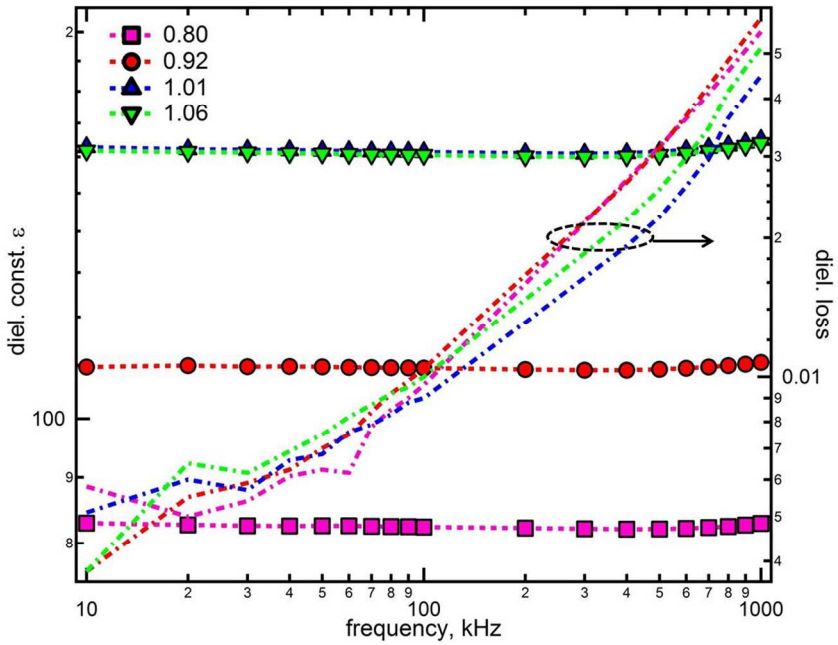

Figure. 8. Frequency dependence of the dielectric constant and the dielectric loss of the four thin films with varying Ba/Ti-ratio.

Similar to ceramics, the most prominent changes occur for the dielectric constant, ε, which strongly depends on the cation ratio as can be seen from Fig. 8 and table 2. The permittivity decreases by more than 50 % from the stoichiometric composition to a Ba/Ti ratio of 0.8. The dielectric constant of 161.6 for the sample with a Ba/Ti-ratio of 1.01 is the highest so far reported for ALD-grown polycrystalline $BaTiO_3$ thin films,[11,46–48] owing to the higher annealing temperature of 750 °C. The equivalent oxide thickness (EOT) as a function of the Ba/Ti-ratio exhibits a similar trend as reported for 12 nm thick as deposited films grown by PE-ALD, where the EOT-values are also lowest close to the stoichiometric composition.[11] However, for the annealed films in this study the minimum is located on the Ba-rich side, whereas the films grown at 250 °C show the lowest EOT-values for Ti-rich films (Ba/Ti-ratio ~0.7).[11] This deviation most likely arises from different dominating influences such as the degree of crystallinity of BTO for PE-ALD-grown films on one hand, and the incorporation of Schottky defects and presence of strain for the annealed films in this work on the other hand.

All samples exhibit an almost frequency independent permittivity with a slight upturn at frequencies of 300 to 400 kHz. Interestingly, the dielectric losses for all samples are very similar in magnitude and frequency dependence, indicating that the relaxation mechanisms are not altered by the composition. Nevertheless, the film with a Ba/Ti-ratio of 1.01 exhibits the smallest losses above 100 kHz, while the losses for the Ti-rich films are largest. In contrast to this observation the dielectric losses increase with the Ba/Ti-ratio in ceramics.[7]

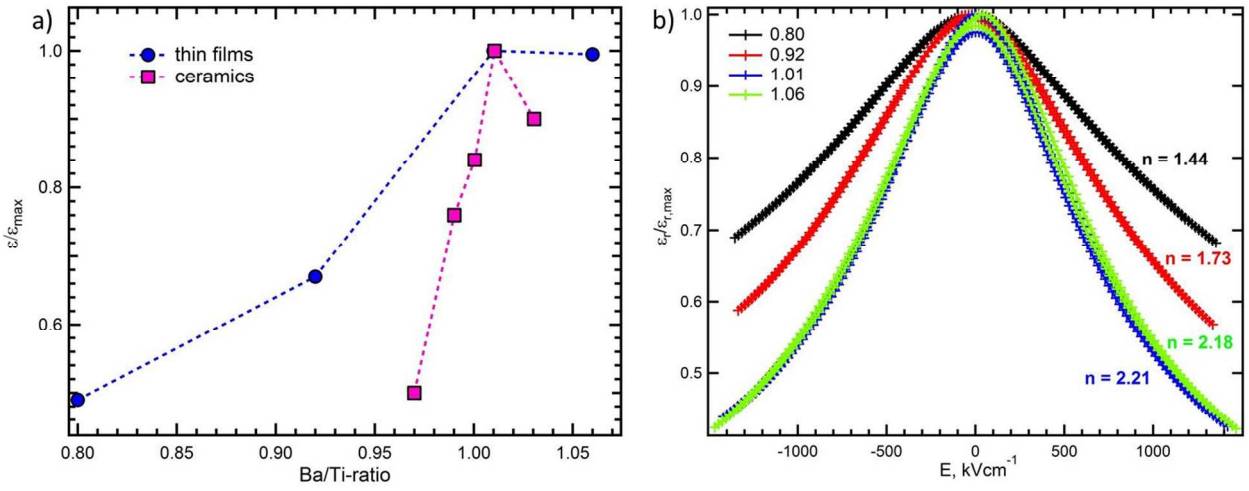

Figure. 9. a) Normalized dielectric constant as a function of Ba/Ti-ratio for the ALD-grown thin films compared to bulk ceramics investigated by Lee *et al*.[7] b) Normalized dielectric constant as a function of electric field for different Ba/Ti-ratios measured at 100 kHz. The tunability for each sample at an electric field of +1300 $kVcm^{-1}$ is provided.

The dependence of the dielectric constant on the Ba/Ti-ratio is very similar to ceramic samples (Fig. 9a).[7] In case of the ceramics, the decrease for the samples furthest from stoichiometry was attributed to the influence of impurity phases with lower permittivity acting as capacitors in series and thereby lowering the overall dielectric constant. For the slightly Ba-rich ceramic sample (Ba/Ti-ratio: 1.01) internal stresses introduced by the thermal mismatch between small impurities of Ba_2TiO_4 and $BaTiO_3$ resulted in the decrease of domain widths leading to an enhanced dielectric constant compared to the stoichiometric composition.[7] Compared to the ceramics an alleviated effect of the cation ratio is present in the thin films (Fig. 9a). The grain sizes in the nm-range for the polycrystalline thin films compared to the µm-range for ceramics account for the ~10 times lower permittivity. [7,16] In addition, the crystallite sizes of 14 nm and below rule out any considerable contributions from domain width. Moreover, on the Ba-rich side the permittivity remains almost constant for thin films. The differences in absolute value of dielectric constants and losses between the ceramics and the thin films imply that different mechanisms are involved. Although the permittivity of $BaTiO_3$ strongly depends on the grain size,[16] the marginal changes in grain and crystallite sizes found for the thin films cannot solely account for the strong dependence of the permittivity on the Ba/Ti-ratio. Due to the lack of impurity phases, the most dominant contribution should arise from Schottky defects within the crystallites in the thin films. From the observed behavior it is apparent that the incorporation of excess TiO_2 rapidly reduces the dielectric constant, whereas additional BaO up to a ratio of 1.06 causes almost no detrimental effects on the permittivity. The increase in lattice parameter with the Ba/Ti-ratio might indicate enhanced internal strain for the Ba-rich films induced by intrinsic defects.

Interestingly, the off-stoichiometry influences not only the absolute value of the dielectric constant, but also the electric field dependence (Fig. 9b). The lack of ferroelectric behavior for all compositions is not surprising, considering the crystallite sizes of 11 to 14 nm and the polycrystalline nature of the films.[16] The tunability, *n*, which is a key parameter for e. g. microwave applications,[49] also decreases significantly as the Ti-content increases. For the stoichiometric and Ba-rich sample the observed values are comparable to PLD-grown polycrystalline 500 nm thick films utilizing liquid phase assisted growth.[50] In order to shed more light on the origin of the strong compositional dependence we applied the Johnson model, which describes the voltage dependence of the permittivity based on the phenomenological Landau-Ginzburg-Devonshire theory in the paraelectric state:[45]

$$(4) \qquad \varepsilon(E) = \frac{\varepsilon(0)}{[1+\alpha\varepsilon(0)^3 E^2]^{1/3}}$$

Here, ε is the dielectric constant, E is the applied electric field, and α is a phenomenological parameter associated with the anharmonic term. Least squares fits to the Johnson model are displayed in Fig. S4 and the values for α are listed in table 2. This constant, which accounts for the anharmonic interaction between Ti-ions, increases with decreasing Ba/Ti-ratio, which is consistent with a larger tetragonal distortion found for Ti-rich ceramics.[9] However, this small increase, which would result in improved tunability, is overcompensated by the larger dielectric constant for more Ba-rich samples.

Conclusions

In summary, we have utilized atomic layer deposition to produce ~50 nm thick nanocrystalline $BaTiO_3$ films on Pt-substrates with varying Ba/Ti-ratio ranging from 0.80 to 1.06. This large cation solubility range is realized after annealing at 750 °C, and is promoted by the small average crystallite sizes ranging between 11 and 14 nm. The presence of the hexagonal polymorph in addition to the perovskite phase was confirmed for all samples by Raman spectroscopy and HRTEM images and emphasizes the metastable state of these thin films. Only subtle differences in structural properties and morphology were observed. These results together with the lack of any Ba- or Ti-rich impurities as well as no cation segregation at the grain boundaries suggest extended metastable solubility for BaO and TiO_2 within the perovskite structure. The solid-solid transformation reaction to form $BaTiO_3$ together with average crystallite sizes of 10 - 15 nm play a decisive role in this solubility enhancement. A detailed evaluation of the cation distribution by EF-TEM corroborates these findings. However, the changes in cation ratio have a strong impact on the physical properties. The systematic changes observed for the leakage current can be explained by the formation of Schottky defects for Ba- and Ti-rich samples. Although the deterioration of the dielectric constant with increasing off-stoichiometry towards Ti-rich compositions is similar to the behavior found for ceramics, the underlying mechanisms are distinctly different and should result from- the defect formation in case of the thin films. The permittivity drops below 50 % of the stoichiometric composition for a

film with a Ba/Ti-ratio of 0.8, and also the tunability is reduced by 35 %. These results emphasize the importance of stoichiometry control for nanocrystalline $BaTiO_3$ thin films to achieve the most desirable properties, e.g. for DRAM or microwave tunable applications.

Conflicts of interest

There are no conflicts to declare.

Acknowledgements

The authors are thankful to Alejandro Gutierrez-Perez for collection of the Raman spectra and to Adrian Podpirka for depositing the top electrodes for the MIM-structures. Work at Drexel University was supported primarily by Office of Naval Research under grant N00014-15-11-2170. I.G. was supported by National Science Foundation (NSF) under grant IIP 1403463. The experiments were partially conducted using the equipment of the Resource Center of Probe and Electron Microscopy (Kurchatov Complex of NBICS-Technologies, NRC "Kurchatov Institute"). We acknowledge the core shared user facilities at Drexel University for access to XRD (NSF DMR 1040166) and Picosun Oy (Finland) for support.

Supporting Information

Detailed information on the fitting results of the X-ray reflectivity data; AFM and SEM images of the sample surfaces and grain sizes extracted from these images; Results of the analysis of the cation distribution from EF-TEM; Evaluation of the conduction mechanism according to the modified Schottky equation; Fitting results of the tunability to the Johnson model.

References:

1 H. H. Sønsteby, H. Fjellvåg and O. Nilsen, *Adv. Mater. Interfaces*, 2017, 1600903.

2 M. D. McDaniel, T. Q. Ngo, A. Posadas, C. Hu, S. Lu, D. J. Smith, E. T. Yu, A. A. Demkov and J. G. Ekerdt, *Adv. Mater. Interfaces*, 2014, **1**, 1400081.

3 J. H. Shim, H. J. Choi, Y. Kim, J. Torgersen, J. An, M. H. Lee and F. B. Prinz, *J. Mater. Chem. C*, 2017, 8000–8013.

4 C. . Levi, *Acta Mater.*, 1998, **46**, 787–800.

5 J.-H. Kim, J.-Y. Kim and S.-W. Kang, *J. Appl. Phys.*, 2005, **97**, 93505.

6 S. Lee, C. A. Randall and Z. K. Liu, *J. Am. Ceram. Soc.*, 2007, **90**, 2589–2594.

7 J. Lee, K. Hong and J.-W. Jang, *J. Am. Ceram. Soc.*, 2001, **84**, 2001–2006.

8 S. Lee, Z. K. Liu, M. H. Kim and C. A. Randall, *J. Appl. Phys.*, 2007, **101**, 1–8.

9 W. P. Chen, Z. J. Shen, S. S. Guo, K. Zhu, J. Q. Qi, Y. Wang and H. L. W. Chan, *Phys. B Condens. Matter*, 2008, **403**, 660–663.

10 J. F. Ihlefeld, P. R. Daniels, S. M. Aygün, W. J. Borland and J.-P. Maria, *J. Mater. Res.*, 2010, **25**, 1064–1071.

11 P. Schindler, Y. Kim, D. Thian, J. An and F. B. Prinz, *Scr. Mater.*, 2016, **111**, 106–109.

12 K. Uchino, E. Sadanaga and T. Hirose, *J. Am. Ceram. Soc.*, 1989, **72**, 1555–58.

13 T. M. Shaw, S. Trolier-McKinstry and P. C. McIntyre, *Annu. Rev. Mater. Sci.*, 2000, **30**, 263–298.

14 M. Yashima, T. Hoshina, D. Ishimura, S. Kobayashi, W. Nakamura, T. Tsurumi and S. Wada, *J. Appl. Phys.*, 2005, **98**, 1–8.

15 S. Lin, T. Lü, C. Jin and X. Wang, *Phys. Rev. B - Condens. Matter Mater. Phys.*, 2006, **74**, 1–5.

16 J. F. Ihlefeld, D. T. Harris, R. Keech, J. L. Jones, J. P. Maria and S. Trolier-McKinstry, *J. Am. Ceram. Soc.*, 2016, **99**, 2537–2557.

17 M. Falmbigl, I. S. Golovina, A. V. Plokhikh, D. Imbrenda, A. Podpirka, C. J. Hawley, G. Xiao, A. Gutierrez-Perez, I. A. Karateev, A. L. Vasiliev, T. C. Parker and J. E. Spanier, *J. Phys. Chem. C*, 2017, **121**, 16911–16920.

18 K. Sakayori, Y. Matsui, H. Abe, E. Nakamura, M. Kenmoku, T. Hara, D. Ishikawa, A. Kokubu, K. Hirota and T. Ikeda, *Jpn. J. Appl. Phys.*, 1995, **34**, 5443–5445.

19 A. Nelson, *J. Appl. Crystallogr.*, 2006, **39**, 273–276.

20 L. Akselrud and Y. Grin, *J. Appl. Cryst.*, 2014, **47**, 803–805.

21 Y. H. Hu, M. P. Harmer and D. M. Smyth, *J. Am. Ceram. Soc.*, 1985, **68**, 372–376.

22 G. V. Lewis and C. R. A. Catlow, *Radiat. Eff.*, 1983, **73 [1-4]**, 307–314.

23 G. V. Lewis and C. R. A. Catlow, *J. Phys. Chem. Solids*, 1986, **47**, 89–97.

24 S. Y. Choi, S. J. L. Kang, S. Y. Chung, T. Yamamoto and Y. Ikuhara, *Appl. Phys. Lett.*, 2006, **88**, 16–18.

25 R. K. Kirby, *Int. J. Thermophys.*, 1991, **12**, 679–685.

26 J. A. Bland, *Can. J. Phys.*, 1959, **37(4)**, 417–421.

27 O. A. Maslova, F. V. Shirokov, Y. I. Yuzyuk, M. El Marssi, M. Jain, N. Ortega and R. S. Katiyar, *Phys. Solid State*, 2014, **56**, 310–316.

28 T. Ohnishi, K. Shibuya, T. Yamamoto and M. Lippmaa, *J. Appl. Phys.*, 2008, **103**, 1–6.

29 D. A. Freedman, D. Roundy and T. A. Arias, *Phys. Rev. B - Condens. Matter Mater. Phys.*, 2009, **80**, 1–13.

30 H. Yamaguchi, H. Uwe, T. Sakudo and E. Sawaguchi, *J. Phys. Soc. Japan*, 1987, **56**, 589–

595.

31 K. Tsuzuku and M. Couzi, *J. Mater. Sci.*, 2012, **47**, 4481–4487.

32 Y. K. V. Reddy, D. Mergel, S. Reuter, V. Buck and M. Sulkowski, *J. Phys. D. Appl. Phys.*, 2006, **39**, 1161–1168.

33 J. P. B. Silva, K. C. Sekhar, A. Almeida, J. A. Moreira, M. Pereira and M. J. M. Gomes, *Appl. Phys. A Mater. Sci. Process.*, 2013, **113**, 379–384.

34 B. Jiang, J. L. Peng, L. A. Bursill, T. L. Ren, P. L. Zhang and W. L. Zhong, *Phys. B*, 2000, **291**, 203–212.

35 U. D. Venkateswaran, V. M. Naik and R. Naik, *Phys. Rev. B*, 1998, **58**, 14257–14260.

36 R. Naik, J. J. Nazarko, V. M. Naik, M. S. Mohammed, G. W. Auner, J. V. Mantese, N. W. Schubring, a. L. Micheli and a. B. Catalan, *Phys. Rev. B*, 2000, **61**, 11367–11372.

37 S. Halder, T. Schneller and R. Waser, *Appl. Phys. A Mater. Sci. Process.*, 2007, **87**, 705–708.

38 C. T. Shelton, P. G. Kotula, G. L. Brennecka, P. G. Lam, K. E. Meyer, J. P. Maria, B. J. Gibbons and J. F. Ihlefeld, *Adv. Funct. Mater.*, 2012, **22**, 2295–2302.

39 K. Chu, J. P. Chang, M. L. Steigerwald, R. M. Fleming, R. L. Opila, D. V. Lang, R. B. Van Dover and C. D. W. Jones, *J. Appl. Phys.*, 2002, **91**, 308.

40 W. Schottky, *Naturwissenschaften*, 1938, **26**, 843.

41 J. G. Simmons, *Phys. Rev. Lett.*, 1965, **15**, 967–968.

42 J. Frenkel, *Phys. Rev.*, 1938, **54**, 647.

43 M. Woehlecke, V. Marrello and A. Onton, *J. Appl. Phys.*, 1977, **48**, 1748–1750.

44 H. Schroeder, *J. Appl. Phys.*, 2015, **117**, 1–13.

45 K. M. Johnson, *J. Appl. Phys.*, 1962, **33**, 2826–2831.

46 M. Vehkamäki, T. Hatanpää, M. Ritala, M. Leskelä, S. Väyrynen and E. Rauhala, *Chem. Vap. Depos.*, 2007, **13**, 239–246.

47 J. An, T. Usui, M. Logar, J. Park, D. Thian, S. Kim, K. Kim and F. B. Prinz, *ACS Appl. Mater. Interfaces*, 2014, **6**, 10656–10660.

48 S. Acharya, J. Torgersen, Y. Kim, J. Park, P. Schindler, A. L. Dadlani, M. Winterkorn, S. Xu, S. P. Walch, T. Usui, C. Schildknecht and F. B. Prinz, *J. Mater. Chem. C*, 2016, **4**, 1945–1952.

49 A. K. Tagantsev, V. O. Sherman, K. F. Astafiev, J. Venkatesh and N. Setter, *J. Electroceramics*, 2003, **11**, 5–66.

50 D. T. Harris, M. J. Burch, J. F. Ihlefeld, P. G. Lam, J. Li, E. C. Dickey and J. P. Maria, *Appl. Phys. Lett.*, 2013, **103**, 1–5.

Graphical Abstract:

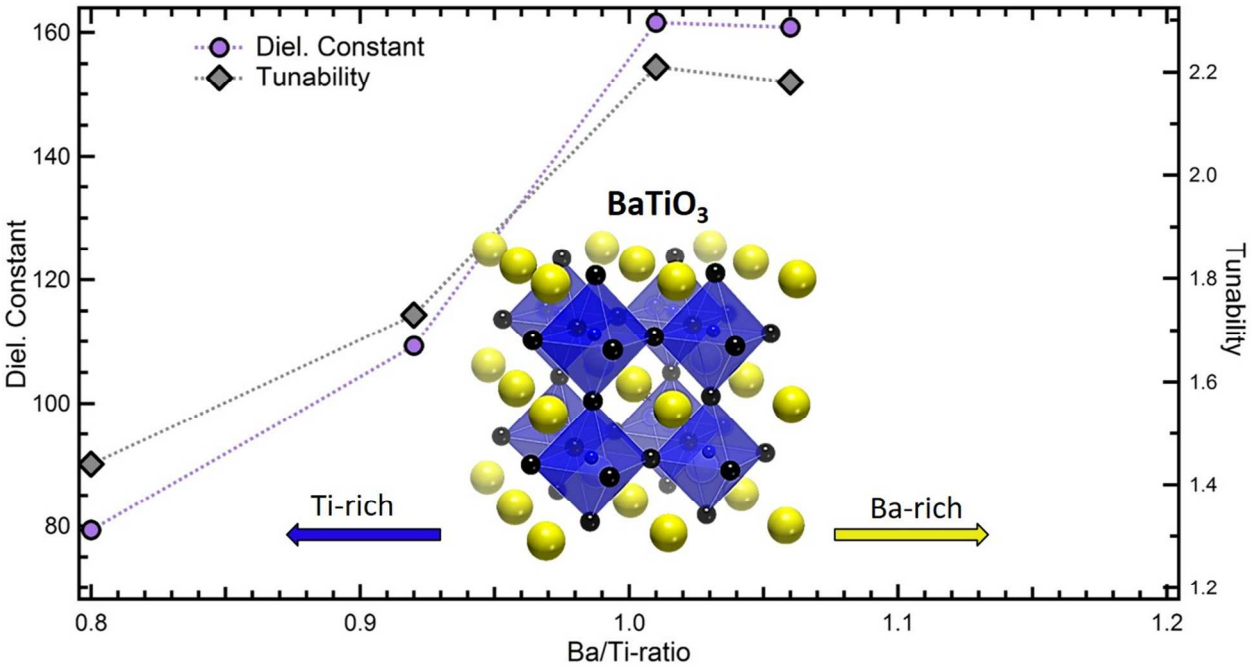

Enhanced cation solubility for atomic layer deposited metastable, nanocrystalline $BaTiO_3$ thin films strongly influences the electrical properties.